frontiers | Frontiers in Nanotechnology

TYPE Original Research
PUBLISHED 23 October 2024
DOI 10.3389/fnano.2024.1483917

OPEN ACCESS

EDITED BY
Emmanuel Emeka Okoro,
University of Port Harcourt, Nigeria

REVIEWED BY
Obumneme Okwonna,
University of Port Harcourt, Nigeria
Zixin Wang,
Los Alamos National Laboratory (DOE), United States

*CORRESPONDENCE
Jan M. Macak,
jan.macak@upce.cz

RECEIVED 20 August 2024
ACCEPTED 14 October 2024
PUBLISHED 23 October 2024

CITATION
Kumar Chennam P, Sepúlveda M, Rihova M, Alijani M, Kachlík M, Zazpe R, Pavlinak D, Maca K and Macak JM (2024) Carbon fibers decorated with TiO_2 nanoparticles for photocatalytic degradation of methylene blue dye. *Front. Nanotechnol.* 6:1483917. doi: 10.3389/fnano.2024.1483917

Carbon fibers decorated with TiO_2 nanoparticles for photocatalytic degradation of methylene blue dye

Pavan Kumar Chennam[1], Marcela Sepúlveda[1,2], Martina Rihova[1], Mahnaz Alijani[1], Martin Kachlík[1], Raul Zazpe[1,2], David Pavlinak[1], Karel Maca[1] and Jan M. Macak[1,2]*

[1]Central European Institute of Technology, Brno University of Technology, Brno, Czechia, [2]Center of Materials and Nanotechnologies, Faculty of Chemical Technology, University of Pardubice, Pardubice, Czechia

This report demonstrates the development of carbon fibers (CFs) decorated with TiO_2 nanoparticles (NPs) as an efficient photocatalyst for the photocatalytic degradation of methylene blue (MB) as a model dye. Carbon fibers were produced by carbonization of polyacrylonitrile fibers, previously produced by centrifugal spinning. Subsequently, the CFs were decorated with TiO_2 NPs (CFs@TiO_2) by tailored soaking protocol using aqueous $TiCl_4$ solution with different concentrations (0.025, 0.05, 0.1, and 0.2 M). SEM analyses revealed that soaking in $TiCl_4$ produced a smooth, conformal, continuous TiO_2 nanoparticulate coating with thickness increasing from 40.4 ± 21.2 to 257.9 ± 63.9 nm with increasing $TiCl_4$ concentration. X-ray diffraction and Raman spectroscopy confirmed the anatase nature of TiO_2. Photocatalytic decomposition rates of MB were assessed under UV light illumination for all CFs@TiO_2 samples, and it was revealed that the lowest amount of TiO_2 NP on C yielded the highest rates. The synergistic interaction between CFs and TiO_2 NPs with a uniform morphology and a well-crystalline anatase structure, present in an optimal amount of fiber bodies, is the key reason for the remarkable photocatalytic performance. This work shows that C fibers decorated with an optimal amount of TiO_2 NPs have a great potential as an effective photocatalytic material.

KEYWORDS

centrifugal spinning, carbon fibers, TiO_2 nanoparticles, decoration, photocatalytic degradation

1 Introduction

Water pollution is a major environmental issue around the world (Parrott et al., 2016; Sobana et al., 2016). Dyes are the most common source of water contamination due to their widespread use in the textile industry, poor biodegradability, and high toxicity (Asiltürk and Şener, 2012). Dyes in wastewater alter the appearance of water and reduce dissolved oxygen levels, both of which have adverse impacts on the ecosystem (Muñoz-Fernandez et al., 2016; Binaeian et al., 2016). Among the dyes used in the textile industry, reactive dyes must be removed by water purification due to their higher concentration and carcinogenic properties (Pandimurugan and Thambidurai, 2016; Mortazavi-Derazkola et al., 2017). Water treatment technologies include flocculation (Lee and Choo, 2014), carbon adsorption

(Malik, 2004), reverse osmosis (Malaeb and Ayoub, 2011), the activated sludge process (Pala and Tokat, 2002), and biological approaches (Bhatia et al., 2017). However, these technologies only transfer contaminants (dyes) from one phase to another, resulting in secondary contamination (Lakshmipathi Naik et al., 2010; Shakouri et al., 2016). As an ideal environmentally friendly technology for the degradation of dye molecules, advanced oxidation processes based on a semiconductor metal oxide photocatalyst have attracted considerable interest in wastewater treatment (Sobana et al., 2016). Photocatalytic processes under ambient conditions (Lin et al., 2015) can degrade many tenacious organic pollutants without adding chemical oxidants. Additionally, photocatalytic degradation is considered as a clean, cost-effective, exceptional reusability, and environmentally beneficial method for the complete degradation of organic dyes (Lee et al., 2015; Farouk et al., 2016).

Metal oxide semiconductors such as iron oxide (Fe_2O_3) (Hitam and Jalil, 2020), titanium dioxide (TiO_2) (Schneider et al., 2014), zinc oxide (ZnO) (Mclaren et al., 2009; Ong et al., 2018) and cerium dioxide (CeO_2) (Samai and Bhattacharya, 2018; Naidi et al., 2021) are frequently used as photocatalysts. Titanium dioxide (TiO_2) is the most widely used metal oxide photocatalyst due to its high stability, low cost, abundance, stability, strong photoactivity, and human and environmental safety (Hir et al., 2017). On the other hand, carbon (C) is a nonmetallic element with a large electron storage capacity. The combination of C and semiconductors, such as TiO_2, produces very interesting mixtures for heterogeneous photocatalytic processes (Takeda et al., 1998; Keller et al., 2005; Shan et al., 2010; Asencios et al., 2022). C accepts photogenerated electrons (e^-_{CB} in semiconductor conductor bands) and holes (h^+_{VB} in semiconductor valence bands) promoting the separation of photogenerated electron-hole pairs, increasing their lifetime. The presence of C can also reduce semiconductor bandgap energy, thus extending light absorption and enhancing its photocatalytic activity (Cui et al., 2013; Teng et al., 2014).

Techniques such as melt-blowing (Hiremath and Bhat, 2015), bicomponent fiber spinning (Naeimirad et al., 2018) electrospinning (Huang et al., 2003), phase separation (Zhao et al., 2011), template synthesis (Ikegame et al., 2003), and self-assembly (Kievsky and Sokolov, 2005) have been used to produce nanofibers. Unlike electrospinning, all of the aforementioned nanofiber production methods have limited applications due to the complexity of fabrication procedures and limited material selections (Lu et al., 2013). The most published approach for producing polymeric and inorganic nanofibers has been electrospinning. However, the high-voltage power supply, dielectric constant sensitivity, extensive amount of solvents, sensitivity to weather, and poor fiber yield restrict its use. These concerns can be efficiently addressed by centrifugal spinning. The benefits of centrifugal spinning have been thoroughly documented in the literature (Sarkar et al., 2010; Rihova et al., 2021) including higher production rates, fewer hazards (the absence of an electrostatic charge capable of igniting organic solutions), improved reproducibility, and dimensional control (Rihova et al., 2021). In recent years, the reproducible production of large amounts of micro - and nanoscale fibers by centrifugal spinning using polymers such as poly (vinylidene fluoride) (Vazquez et al., 2012), polycaprolactone (McEachin and Lozano, 2012), nylon6 (Mihut et al., 2014), biopolymers (Rihova et al., 2022), or forming inorganic fibers, such as tungsten trioxide (Hromádko et al., 2021), silicon dioxide (Hromádko et al., 2017), cobalt (II, III) oxide (Ayala et al., 2021), aluminum oxide (Natarajan and Bhargava, 2018), etc., has been shown to be very successful.

During the centrifugal spinning process (Hromádko et al., 2017), a strong centrifugal force acts on the spinneret precursor to push the fibers out. Optimized circulation from the air inlet to the air outlet in the spinning chamber expedites the solvent's evaporation, leaving the fibers behind, on a fiber collector, where these fibers are collected. Theoretically, the most important factors affecting fiber yield are the spinneret speed, the collector distance, and the diameter of the spinneret nozzle Furthermore, the viscosity of the solution, the spinneret's rotational speed, and the evaporation rate significantly influence the fibers' morphology and size (Rihova et al., 2021). Depending on the process settings and spinning solution employed, fibers with diameters ranging from a few hundred nanometers to a few micrometers can be generated.

In this work, we report the decoration of CFs with TiO_2 NPs (CFs@TiO_2) by immersing them in aqueous $TiCl_4$ solutions with various concentrations of and a post-annealing process at 400 °C for 30 min TiO_2 decorated samples were examined by using X-ray diffraction (XRD), scanning electron microscopy (SEM), energy dispersive X-ray analysis (EDX), ultraviolet-visible diffuse spectroscopy (UV-Vis), Raman spectroscopy (RS), and Photoluminescence spectroscopy (PL). The synthesized TiO_2 NPs decorated samples were compared with commercially available reference TiO_2 nanofibers produced by electrospinning (TiO_2@ ES) for photodegradation of methylene blue dye under UV irradiation (λ = 365 nm).

2 Materials and methods

2.1 Materials

DOLAN GmbH, Germany, supplied polyacrylonitrile granulate (molecular weight 116,000 g/mol, N-PAN). Penta Chemicals (Czech Republic) provided N, N-dimethylacetamide (DMAC, min. 99.5 wt %), which was used as a solvent for PAN. $TiCl_4$ for synthesis was provided by Sigma-Aldrich. Other chemicals (H_2SO_4, $KMnO_4$, H_3PO_4) mentioned in this work were purchased from Sigma-Aldrich.

2.2 Centrifugal spinning of polyacrylonitrile (PAN)

At room temperature, PAN was dissolved in DMAC by stirring with magnetic stirrers. The solution was prepared at a concentration of 15 wt%. The total weight of the PAN solution intended for the spinning process on Cyclone Pilot G1 (centrifugal spinning pilot tool, Pardam Nano4Fibers Ltd., Czech Republic) was 300 g (Hromádko et al., 2017). The following processing conditions were used for fiber production: 10,000 rpm rotational speed, 35°C ± 5°C temperature, and 25% ± 5% relative humidity (RH). The resulting fibers were collected and dried in air in the form of bulky 3D structures. The efficiency of the production process was approximately 70%, corresponding to 32 g of dry nanofibrous material.

2.3 Carbonization processes

The process of obtaining CFs was described in the previous work (Chennam et al., 2024). In brief, to stabilize the PAN fibers, they were heated in an XERION XRETORT 1200 furnace at 240°C for 60 min, with a ramp rate of 1°C.min^{-1}. The stabilized fibers were carbonized in an argon environment at 900°C, with a heating rate of 5°C.min^{-1}. After the optimal temperature for carbonization was reached, the furnace was left to naturally cool down to ambient temperature.

2.4 Chemical surface treatment

CFs are hydrophobic by nature; therefore, an acid treatment was used to improve their wettability (hydrophilic nature) (Marcano et al., 2010; Thalluri et al., 2023). The Marcano-Tour method (Marcano et al., 2010) was used to treat the CFs. 170 mg of $KMnO_4$ (potassium permanganate) and 9:1 (v/v ratio) solution of H_2SO_4 (sulfuric acid)/H_3PO_4 (phosphoric acid) solution were used for the conventional Marcano-Tour procedure. Using a temperature-controlled water bath, the mixture was heated to 45 °C and stirred continuously for 24 h. Finally, they are dried in the oven at 60°C.

2.5 Decoration of CFs with TiO_2

To obtain CFs decorated with TiO_2 NPs, the CFs were immersed in ice-cooled solutions of deionized (DI) water and titanium tetrachloride ($TiCl_4$) of various concentrations (0.025, 0.05, 0.1, and 0.2 M). 30mg of the CFs were immersed in a solution that was 1 mL in volume. Following immersion, the samples were subjected to sonication for 1 min in an ultrasonic bath to ensure uniform dispersion. Subsequently, the fibers were soaked in a temperature-controlled water bath (70°C, 30 min), drying (70°C, 30 min) (Sopha et al., 2017). Finally, the annealing process was carried out in a muffle oven at 400°C for 30 min in a static air environment, with a heating rate of 2.1°C·min^{-1} to obtain the structure of anatase (Sopha et al., 2020).

2.6 Photodegradation tests

Photocatalytic experiments were performed following the relevant processing parameters reported in previous work (Hromádko et al., 2021). For all these experiments, 10 mg of each sample was employed. On the basis of prior experience and preliminary experiments, this amount of fibers was determined to be the best match for accurately depicting the differences in degradation rates among the samples. Photocatalytic degradation of the methylene blue (MB) solution (initial concentration = 1 × 10^{-5} M) was used to evaluate the photocatalytic activities of CFs decorated with TiO_2 NPs using various concentrations of $TiCl_4$. As a reference, commercial TiO_2 nanofibers produced by electrospinning (TiO_2@ES) were used (gift sample from PardamNano4Fibers Ltd.). To establish the equilibrium between dye adsorption and desorption, 10 mg of CFs decorated with TiO_2 NPs were soaked in 30 mL of MB solution for 1 h in the dark with constant stirring at 300 rpm. After equilibrium was reached, all fibers were irradiated with an LED-based UV lamp (10 W) using the particular wavelength of λ = 365 nm. nn The degradation rates were monitored by measuring the absorbance of the MB solution every 10- or 30-min steps using a visible light spectrophotometer (S-200, Boeco). Before absorbance measurements, carbon and pure TiO_2 fibers were separated from the MB solution using a combination of ultracentrifugation at 15,000 rpm for 5 min at 25°C using a fixed angle rotor (MLA-50) and a high-speed centrifuge (Fisherbrand, HSE09225) at 11,000 rpm for 3 min.

2.7 Characterization techniques

Using a field emission scanning electron microscope (SEM, FEI, Verios 460 L) with an acceleration voltage of 5 kV, the surface morphology of CFs and CFs decorated with TiO_2 NPs using various concentrations of $TiCl_4$ were observed. Average TiO_2 coating thicknesses were determined using Nanomeasure from cross-sectional SEM images. A minimum of 100 measurements were made using three or four SEM images. A Tescan MIRA3 XMU scanning electron microscope equipped with an energy-dispersive X-ray detector (Oxford Instruments, United Kingdom) at an acceleration voltage of 7 kV was used to analyze the elemental composition. The structure of the samples was evaluated using an X-ray diffractometer (XRD; Smart Lab 3 Kw from Rigaku, Japan), which was set in Bragg-Brentano geometry with Cu-Kα radiation (λ = 0.154 nm) and fitted with the Dtex-Ultra 1D detector. A 30-Ma current and 40 kV were employed to power the Cu radiation. The diffraction patterns were captured from 10° to 90° with a step size of 0.01° and a scan speed of 4° min^{-1}. Diffuse reflectance spectroscopy (DRS) measurements were performed in the wavelength range of 200–800 nm using a UV-visible-NIR Jasco V-770 spectrometer with a 16 mm diameter Spectralon-coated integrating sphere and 1 nm spectral resolution. Each sample was deposited in a quartz cuvette, sealed, and mounted in a sample holder. Raman spectroscopy (RS) was performed on CFs with and without decoration using a Witec alpha300R spectroscope (WITec, Ulm, Germany). In the Raman shift range of 100–2000 cm^{-1}, spectra were obtained in continuous scanning mode at a laser excitation wavelength of 532 nm. The laser beam was focused using a ×100 objective lens, resulting in a 1 μm diameter point. The measurement signal was reconstructed using five accumulations and a 20-s integration time. The photoluminescence (PL) measurements were conducted using a WITec Alpha 300R instrument equipped with a 355 nm excitation laser operating at a power of about 3.89 mW. A ×40 objective lens with a numerical aperture (N.A.) of 0.6 was used.

3 Results and discussion

3.1 Morphological analysis

Figure 1 shows SEM images of the CFs samples with and without TiO_2 nanoparticulate coatings. The morphology of all CF is fibrous, and remains fibrous, even when used as a substrate for subsequent

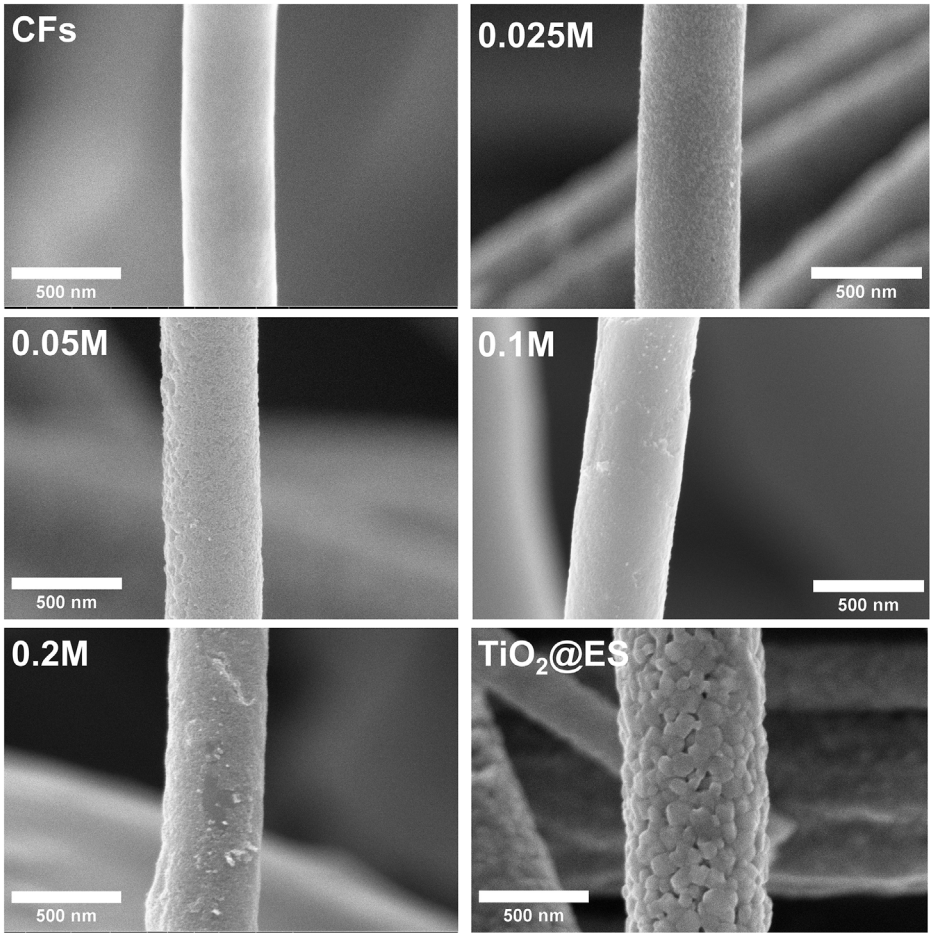

FIGURE 1
SEM images of CFs, CFs decorated with TiO_2 NPs using various concentrations of $TiCl_4$ and reference TiO_2@ES fibers.

deposition of TiO_2 nanoparticles (NPs). The average diameter of the CF is 1.4 ± 0.21 μm, based on the measurement of 100 counts (N = 100) and statistical evaluation. As can be seen, the concentration of $TiCl_4$ in the soaking solution has a significant effect on the resulting amount of the TiO_2 NPs on the CF. It can be seen that the TiO_2 film is composed of NPs that have covered the surface of the CFs using various concentrations (0.025, 0.05, 0.1, and 0.2 M) of $TiCl_4$. For the 0.025 M case, decoration resulted in a smooth, uniform, and continuous TiO_2 nanoparticulate coating with negligible peeling. For higher concentrations of $TiCl_4$, peeling of deposited TiO_2 nanoparticulate coating was observed on some spots, which indicated rather limited adhesion of TiO_2 on CFs, which may be attributable to the excessive thickness of the TiO_2 nanoparticulate coating resulting from an excessively high $TiCl_4$ concentration. However, the peeling was observed only, when samples were mechanically pressed, such as for the SEM inspection on the SEM stub. No significant peeling was observed when the samples were employed in photocatalysis without external applied pressure. TiO_2 fibers produced by electrospinning (TiO_2@ES) showed a smooth fiber surface, free of defects, cracks, or other imperfections.

The thickness of CFs decorated TiO_2 nanoparticulate coatings was estimated from the cross-sectional SEM images (Figure 2). The thickness of TiO_2 coatings were 40.4 ± 21.2, 76.5 ± 28.1, 185.4 ± 63.5, and 257.9 ± 63.9 nm, respectively, for 0.025, 0.05, 0.1 and 0.2 M $TiCl_4$ solutions. Overall, the sample with 0.2 M showed the highest thickness, as expected. Supplementary Figure S1 in SI shows the overall morphology of CFs with and without TiO_2 nanoparticulate coatings at a low magnification.

3.2 EDX analysis

EDX analyses were performed to analyze the composition of CFs that have been decorated with TiO_2 NPs using various concentrations of $TiCl_4$. EDX examinations were carried out at four distinct locations on each sample to ensure that the elements were evenly distributed. The statistically enriched results are outlined in Table 1. The following table shows that the only element present in CFs is carbon. The TiO_2 NPs decorated samples exhibit the presence of titanium (Ti), oxygen (O), and carbon (C). The EDX results for sample 0.2 M in Table 1 confirm this, showing that Ti and O were present in higher quantities, while C was present in lower quantities. The relatively low percentage of carbon implies that most of the surface of the CFs was covered with TiO_2.

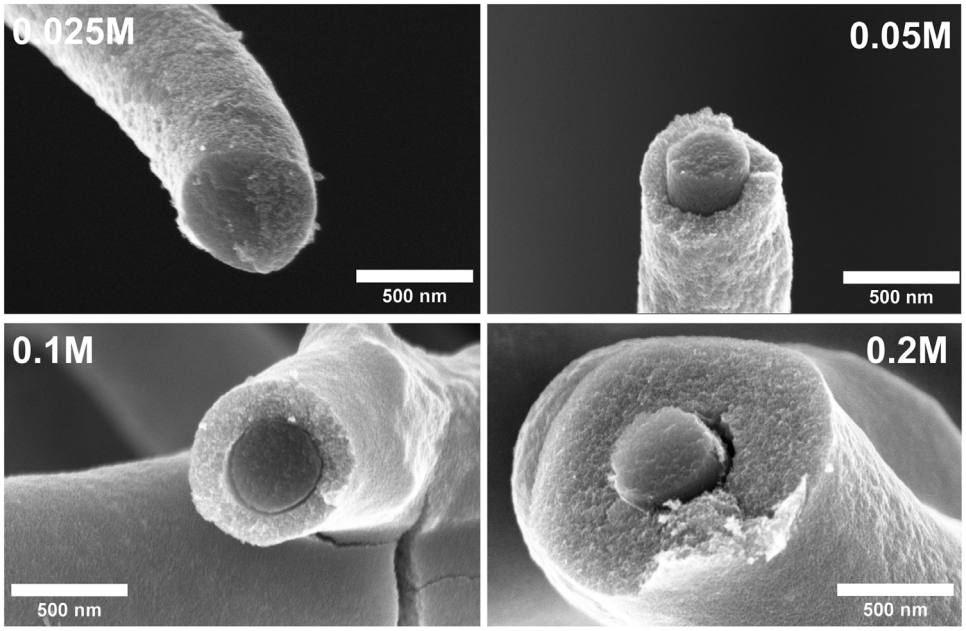

FIGURE 2
Cross-sectional SEM images of CFs decorated with TiO_2 NPs using various concentrations of $TiCl_4$.

TABLE 1 EDX analyses of CFs and CFs decorated TiO_2 NPs using various concentrations of $TiCl_4$.

Sample ID	Mass content (wt%)		
	Ti	O	C
CFs	—	—	100.00
0.025 M	44.55 ± 2.19	8.09 ± 0.9	47.36 ± 3.05
0.05 M	48.58 ± 2.19	10.24 ± 2.42	41.18 ± 4.55
0.1 M	55.62 ± 2.15	13.92 ± 0.98	30.46 ± 2.80
0.2 M	58.00 ± 2.58	16.62 ± 2.41	25.40 ± 4.91

3.3 Crystallinity analysis

Figure 3 shows the XRD patterns of CFs and CFs decorated with TiO_2 NPs(CFs@TiO_2) using various concentrations of $TiCl_4$. As one can see from Figure 3 there are two broad bumps for the CFs at approximately 26° and 45° that could be assigned to the (002) and (101) planes of graphite (Cao et al., 2019) respectively. For all CFs@TiO_2 samples, these broad bumps are no longer visible, which is attributable to the presence of TiO_2 on CF bodies, which is responsible for the weakening of the CF diffraction peaks.

For CFs@TiO_2 (0.025 M), the XRD pattern exhibits one TiO_2 apparent diffraction peak at about 25.7° that becomes increasingly intense with increasing $TiCl_4$ concentration. Six additional diffraction peaks appear in the XRD pattern of CFs@TiO_2 (0.2 M). The diffraction peaks at 25.7°, 38.4°, 48.4°, 55°, 63.1°, 69.9°, and 75.7° match the crystal faces (101), (004), (200), (105), (213), (116) and (215) of anatase TiO_2 [JCPDS # 75–1537]. Using Scherrer's equation (Langford and Wilson, 1978) for the diffraction peak at 25.7° (which corresponds to the main anatase (101) peak), the crystallite size of CFs decorated TiO_2 NPs using various concentrations (0.025, 0.05, 0.1, and 0.2 M) of $TiCl_4$ were calculated and was found to be 3.6, 4.9, 7.3, and 9.1 nm, respectively. Supplementary Figure S2 illustrates an additional XRD pattern of the reference TiO_2 fibers generated through electrospinning (TiO_2@ES). The power law relationship $D = K.T^n$ (Dulmaa et al., 2021) was used to illustrate the relationship between the crystallite size (referred to as D) and the thickness of the TiO_2 layer (referred to as T) for CFs @ TiO_2. In this equation, D represents the crystallite size, T represents the thickness, n represents the growth exponent, and K is the proportionality constant. It demonstrates that when the concentration of $TiCl_4$ increases from 0.025 M to 0.2 M, the crystallite size increases in proportion to the square root of the thickness. More information about this relationship is available in Supplementary Table S1 in the Supplementary Material.

3.4 Raman analysis

Raman spectroscopy (RS) is a versatile technique for identifying the phase composition, the defect concentration of the materials (Kiran and Sampath, 2012), etc. Since the carbon information was not well defined by XRD patterns (Figure 3) for CFs@TiO_2 NPs, the aim of RS measurements was to investigate whether there are any structural changes in the CFs observed after the TiO_2 NPs decoration on CFs. Figure 4 shows the RS of blank CFs and CFs@TiO_2 NPs.

The RS of the CFs decorated with TiO_2 NPs using different concentrations of $TiCl_4$ exhibits four peaks with strong intensities at 150 (E_g), 395 (B_{1g}), 515.3 (A_{1g}) and 642 (E_g) cm^{-1}, which are

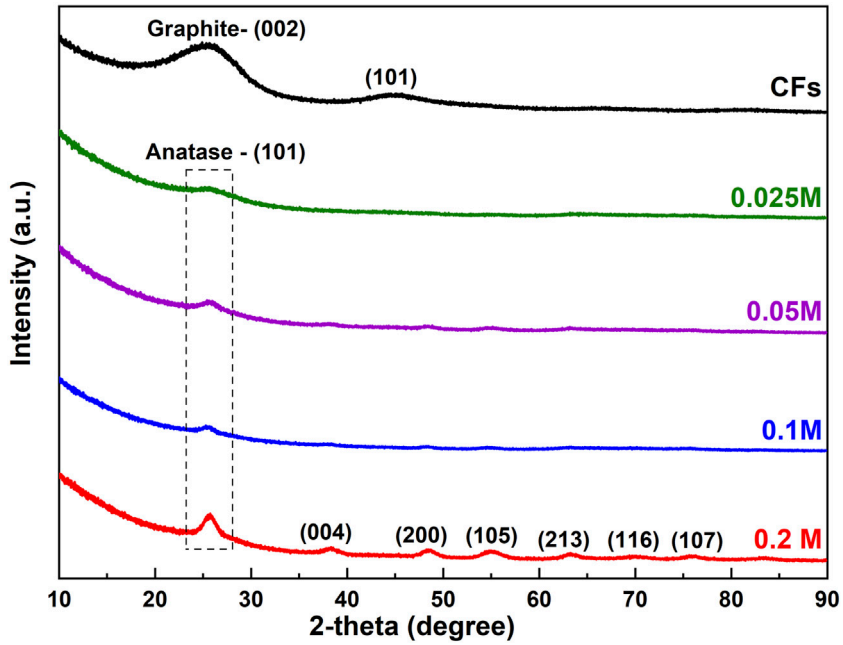

FIGURE 3
XRD patterns of CFs and CFs decorated by TiO_2 NPs using various concentrations of $TiCl_4$.

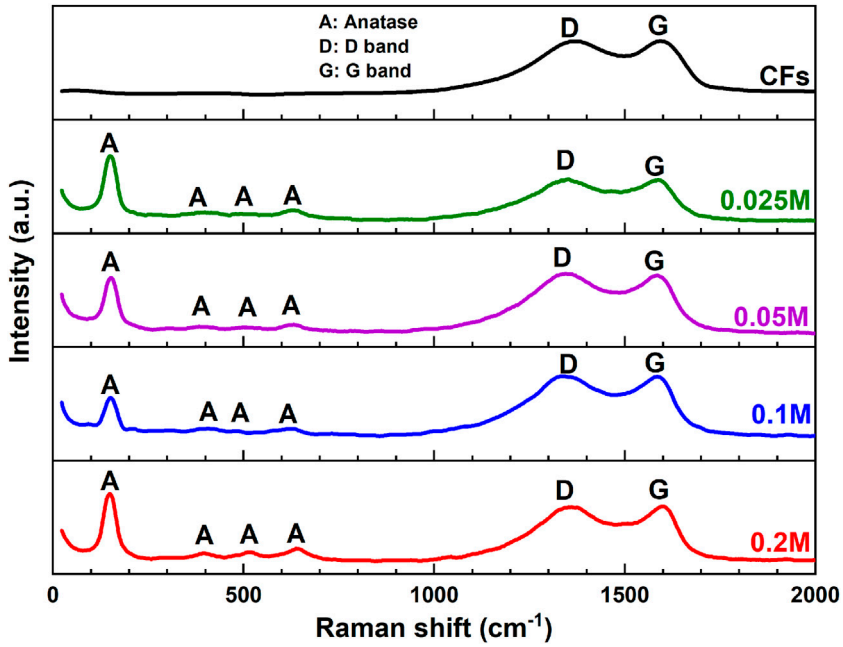

FIGURE 4
Raman spectra of CFs and CFs decorated with TiO_2 NPs using various concentrations of $TiCl_4$.

consistent with those of published anatase TiO_2 (Yanagisawa and Ovenstone, 1999; Liu et al., 2015). The strongest E_g mode at 150 cm^{-1} is clearly visible and can be attributed to the external vibration of the anatase phase (Appadurai et al., 2019). RS also confirms the existence of carbon for CF@TiO_2. The spectra reveal the existence of two bands, one near 1580 cm^{-1} (G band) attributed to a graphitic structure with sp^2 hybridization, while another near 1350 cm^{-1} (D band) represents defects present in the hexagonal graphitic structure (Cai et al., 2020). The observed increase in the I_D/I_G intensity ratio was between 0.99 and 1.02 for CFs@TiO_2 NPs using different concentrations of $TiCl_4$, respectively, demonstrating that the addition of TiO_2 could lead to more defects (Ye et al., 2022).

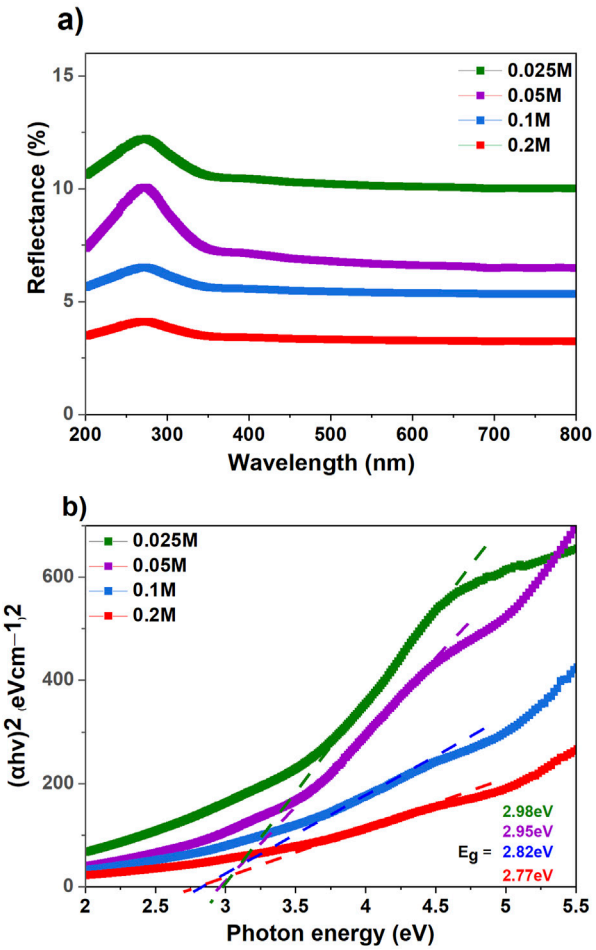

FIGURE 5
(A) UV-Vis diffuse reflectance spectra (DRS) of CFs decorated TiO_2 NPs and **(B)** Kubelka-Munk curves for an estimation of the optical band gap for CFs decorated TiO_2 NPs using various concentrations of $TiCl_4$.

3.5 UV-vis analysis

The UV–Vis diffuse reflectance spectroscopy (DRS) was used to acquire the UV–Vis reflectance spectra of CFs@TiO_2. As shown in Figure 5A, the reflectance spectra of CFs decorated with TiO_2 provided a redshift (to longer wavelengths), extending their response from UV (200–400 nm) to visible (400–800 nm) regions.

The diffuse reflectance (R) is converted to an equivalent F(R) absorption coefficient using the Kubelka-Munk (Equation 1)

$$\mathbf{F(R)} = \frac{(1\text{-}2R)^2}{2R} \quad (1)$$

where R corresponds to the reflectance of the sample and F(R) is the absorbance. The band gap energy ($E_{g.}$) in Figure 5B was calculated by extrapolating the linear part of the Tauc plot and intersecting it with the abscissa axis. Supplementary Figure S3 shows the reflectance spectra and bandgap energy ($E_{g.}$) of the reference TiO_2 fibers produced by electrospinning (TiO_2@ES). The band gap energy calculated for TiO_2@ES is about 3.14 eV, typical for TiO_2 (3.0–3.2 eV) (Fujishima et al., 2008). The optical bandgap of

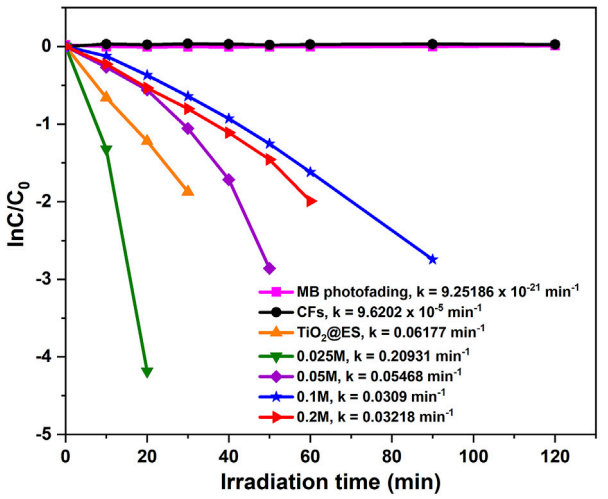

FIGURE 6
Photocatalytic degradation kinetics curves of MB for CFs decorated TiO_2 NPs and their corresponding rate constants.

CFs decorated with TiO_2 NPs using various concentrations of 0.025, 0.05, 0.1, and 0.2 M was 2.98 eV, 2.95 eV, 2.82 eV, and 2.77 eV, respectively. It has been demonstrated that increasing the thickness (Ghemid et al., 2021), the crystallite size (Ghemid et al., 2021), and the chemical interaction between TiO_2 and CFs (El-Sayed et al., 2019) leads to a decrease in the band gap energy.

3.6 Photocatalytic activity

The photocatalytic activities of CFs decorated TiO_2 NPs using various concentrations of $TiCl_4$ and reference TiO_2 fibers (TiO_2@ES) were investigated for the photodegradation of MB under UV light illumination (λ = 365 nm). As one can see, CFs decorated with different TiO_2 NPs amount needed different degradation times. As part of our standard process conditions, during the first hour, measurements were taken every 10 min, which accurately captured the degradation process. For samples with rather poor performance, after the first hour, photodegradation significantly slowed down, therefore, the measurement intervals were increased to 30 min (this applies to the photofading, CFs, 0.025 M, 0.05 M, 0.1 M, and 0.2 M $TiCl_4$ concentration).

During the photocatalytic degradation of methylene blue, both oxidation reactions (driven by holes and reactive oxide species (ROS)) and reduction reactions (driven by electrons) happen at the same time. When these processes work together, they break down methylene blue into CO_2, water, and other less dangerous substances (Rajeshwar et al., 2008). Considering the shape of the resulting photocatalytic degradation curves, the photocatalytic degradation was governed by first-order kinetics. The expression for kinetics is as follows: $\ln (C/C_0) = k_a t$ (Yu et al., 2007).

The photocatalytic degradation was governed by first-order kinetics. The expression for kinetics is as follows: $\ln (C/C_0) = k_a t$. The linear relationship between $\ln (C/C_0)$ and time is illustrated in Figure 6, where C_0 ($mg{\cdot}L^{-1}$) and C ($mg{\cdot}L^{-1}$) represent the initial and residual concentrations of MB, respectively, t is the reaction time

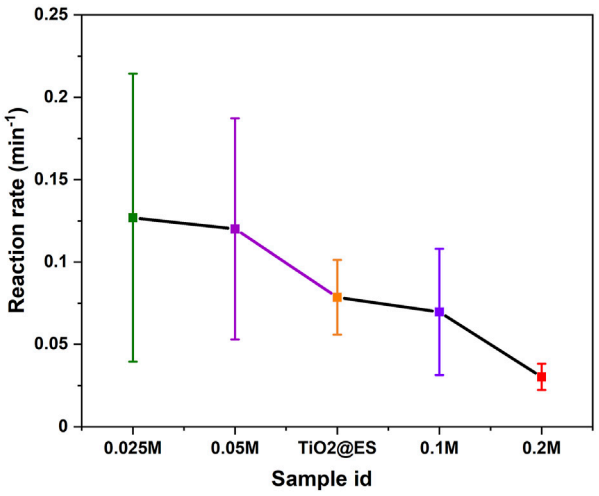

FIGURE 7
Variation of MB degradation rates for CFs@TiO_2 NPs and reference TiO_2@ES fibers.

and k_a is the reaction rate constant. The photocatalytic results for CFs, TiO_2@ES, 0.025 M, 0.05 M, 0.1 M, and 0.2 M reveal the degradation rates of MB ($k = 9.6202 \times 10^{-5}$, 0.06177, 0.20931, 0.05468, 0.0309 and 0.03218 min^{-1}, respectively). This means that the reference pure TiO_2@ES fibers provided the second-highest degradation rate after the 0.025 M CFs@TiO_2 sample in this particular experiment. Furthermore, the linear correlation coefficients (R^2) for the CFs, TiO_2@ES and 0.025 M, 0.05 M, 0.1 M, and 0.2 M CFs@TiO_2 sample were 0.11927, 0.99908, 0.9566, 0.92275, 0.98298, and 0.9836. For all CFs@TiO_2, the correlation coefficients (R^2) found were greater than 0.92, indicating that the first-order kinetic equation fits the experimental data quite well.

Figure 7 shows an overall photocatalytic trend, obtained from the statistical evaluation of three different photodegradation experiments. The results of the statistical distribution for Figure 7 for samples with concentrations of 0.025 M, 0.05 M, TiO_2@ES, 0.1 M, and 0.2 M were 0.1269 ± 0.08744, 0.12011 ± 0.0671, 0.07856 ± 0.02272, 0.06965 ± 0.03833, and 0.03022 ± 0.00791, respectively. It confirms that 0.025 M samples have the highest photocatalytic activity even in this comparison. The reaction rate of 0.025 M samples is 1.6 times that of the TiO_2@ES samples. However, in this statistically rich representation, the 0.05 M samples were also better than the reference TiO_2@ES. Based on previous studies, crystallite size (Allen et al., 2018), crystalline structure (Tsai and Cheng, 1997), and surface area and mass of TiO_2 (which translates into a thickness of the TiO_2 nanoparticulate coating in this case) (Wu et al., 2013) are crucial factors that influence photocatalytic activity. These parameters are quite sensitive to the preparation procedures and deposition conditions (Smirnov et al., 2010).

The rate of photocatalytic degradation is mainly determined by the number of reactive species generated, which is influenced by the surface of the photocatalyst and the separation of electrons and holes. The more efficiently electrons and holes are separated and the larger the surface of the photocatalyst, the more reactive species are produced, leading to a faster degradation rate (Gaya and Abdullah, 2008; Henderson, 2011). The 0.025 M CFs@TiO_2 sample likely has a lower specific surface area (not measured though and difficult to measure due to an extensive mass needed for that) compared to the pure TiO_2@ES fibers, thus, its better performance can be assigned rather to a better separation of electrons and holes.

In order to provide additional insight, the photocatalytic performance was further investigated in the presence of methanol, which is well known to act as a hole and a hydroxyl radical scavenger (Prakash et al., 2016; Djellabi et al., 2017; Parvizi et al., 2019). The photocatalytic degradation kinetics curves of methanol for CFs@TiO_2 samples and reference TiO_2@ES fibers are depicted in Supplementary Figure S4. As can be seen there, the photodegradation rates decreased in the presence of methanol for the lowest TiO_2 content (0.025 M CFs@TiO_2 sample), whereas it almost did not decrease for all other CFs@TiO_2 samples and the reference TiO_2@ES fibers. This confirmed that for the least decorated CFs@TiO_2 sample (i.e. 0.025 M), the photocatalytic activity is governed mainly by •OH radicals created from holes and very minorly by superoxide anion (O_2^-) created from the interaction of oxygen and electrons. However, in the case of TiO_2@ES fibers and other decorated CFs@TiO_2 (such as 0.2 M) the photocatalytic degradation effect is mainly governed by superoxide anion (O_2^-) because the use of scavenging methanol did not have any significant effect.

Moreover, it is also evident from the photoluminescence (PL) analysis (Supplementary Figure S5) that the 0.025 M sample experienced a low PL intensity. This could be attributed to good surface contact between two materials (CFs and TiO_2) that may have contributed to charge separation. As a result, the peak intensity for sample 0.025 M was significantly reduced, suggesting that CFs could prevent photoelectrons and holes from recombining (Chandra et al., 2018; Tahir et al., 2023) and thus increase the photocatalytic activity.

Crystallite size has been recognized as one of the factors influencing photo-reactivity since it affects multiple physical attributes, such as surface area, surface energy, light absorptivity, and lattice distortion (Swamy et al., 2006; Henderson, 2011). On the basis of the XRD findings, the highest photocatalytic activity (sample 0.025 M) was observed with the lowest crystallite size (3.6 nm). Similarly, it has been reported that the smallest crystallite size has been shown to give the highest photocatalytic hydrogenation of propyne (Anpo et al., 1987). As a result of the quantum confinement effect, it has been stated that the energy of photo-generated radicals increases with decreasing crystallite size, thereby increasing photocatalytic activity (Wang et al., 2014). This has been further supported by other authors who have studied several other photoreactions (Yeung et al., 2002). Furthermore, it has been reported that a smaller crystallite size leads to a higher surface area, which improves the absorption of the reactants and then improves the photo-reactivity (Xu et al., 1999; Xie et al., 2010).

Several studies have shown that the photocatalytic activity of thin films depends on thickness (Quici et al., 2010; Davisdóttir et al., 2014; Kenanakis et al., 2015). However, in this work, such a direct trend was not observed. Based on the SEM cross-sectional images (Figure 2) and photocatalytic experiments conducted in this work, the sample 0.025 M with a TiO_2 nanoparticulate layer thickness of 40.4 ± 21.2 nm showed the highest photocatalytic activity. An additional increase in thickness for the samples from 0.05 M to 0.2 M led to a decrease in photocatalytic activity, although the

penetration depth of UV-vis light increased and the mass of TiO_2 also increased. This clearly shows that it is the interplay between C and TiO_2 that plays a major role, rather than other parameters (Wu et al., 2013). This observation is in good agreement with previously reported findings (Subramanian et al., 2003; Malagutti et al., 2009; Kumar et al., 2011). In addition, the current study identifies factors that could influence the photocatalytic degradation of methylene blue, including the concentration of TiO_2 on CFs, poor adhesion of TiO_2 on CFs, inadequate light penetration, higher recombination rates, and the generation of degradation intermediates. This study showed that structural properties and thickness have a significant impact on the photocatalytic activity of carbon fibers decorated with TiO_2 NPs using various concentrations of $TiCl_4$.

4 Conclusion

In this study, PAN fibers (produced by centrifugal spinning) were stabilized and then carbonized at 900°C to produce CFs. Subsequently, the CFs were decorated with TiO_2 NPs nanoparticles by soaking in $TiCl_4$ solutions with different concentrations (0.025, 0.05, 0.1, and 0.2 M) and subsequent annealing at 400°C for 30 min. SEM, EDX, UV-Vis, XRD, and Raman analyses were used to examine the resulting CFs@TiO_2 materials. According to SEM analysis, TiO_2 peeling occurred for 0.05, 0.1 M, and 0.2 M samples, while did not appear for the 0.025 M sample, which led to defect-free homogeneous TiO_2 nanoparticulate coatings on carbon fiber bodies without flaking. EDX analysis showed that 0.2 M had a relatively low carbon content, which means that most of the CF surface was covered by TiO_2 nanoparticulate coating. The UV-Vis DRS showed that an increase in $TiCl_4$ concentrations of 0.025 M to 0.2 M leads to a drop in the optical band gap energy from 2.98 eV to 2.77 eV. XRD reveals that the intensity of the TiO_2 diffraction peak increases with $TiCl_4$ concentration from 0.025 M to 0.2 M. The crystallite size increases linearly from 3.6 to 9.6 nm for 0.025 M to 0.2 M samples. RS was used to investigate the changes observed after TiO_2 decoration on CFs. RS of CF@ TiO_2 NPs reveals four strong peaks at 150, 395, 515, and 642 cm^{-1}, confirming the presence of the anatase phase. The I_D/I_G ratio increases from 0.99 to 1.02 after TiO_2 loading, demonstrating that the addition of TiO_2 could lead to more defects. The results of the photocatalytic activity for $TiCl_4$ concentrations ranging from 0.025 M to 0.2 M revealed that the sample 0.025 M exhibits the highest photocatalytic activity, which is 1.6 times greater than that of the reference TiO_2 fibers produced by electrospinning (TiO_2@ES), which themselves are good photocatalyst, according to our measurements and available literature. This may be attributed to the presence of a uniform and defect-free morphology of TiO_2 on the surface of CFs.

Data availability statement

The raw data supporting the conclusions of this article will be made available by the authors, without undue reservation.

Author contributions

PK: Conceptualization, Data curation, Investigation, Methodology, Writing–original draft. MS: Data curation, Investigation, Writing–original draft. MR: Data curation, Investigation, Writing–review and editing. MA: Data curation, Methodology, Writing–review and editing. MK: Investigation, Methodology, Writing–review and editing. RZ: Methodology, Writing–review and editing. DP: Data curation, Investigation, Writing–review and editing. KM: Resources, Supervision, Writing–review and editing. JM: Conceptualization, Methodology, Resources, Supervision, Writing–review and editing.

Funding

The author(s) declare that financial support was received for the research, authorship, and/or publication of this article. The authors were supported by the Ministry of Education, Youth and Sports of the Czech Republic (projects LM2023037 and LM2023051).

Acknowledgments

The authors gratefully acknowledge support from the Ministry of Education, Youth and Sports of the Czech Republic for the support of the Large Research Infrastructures Czech Nano Lab (project LM2023051) and CEMNAT (project LM2023037) used for the materials characterization and fiber synthesis, respectively. We thank Veronika Cicmancova for providing the PAN fibers.

Conflict of interest

The authors declare that the research was conducted in the absence of any commercial or financial relationships that could be construed as a potential conflict of interest.

The author(s) declared that they were an editorial board member of Frontiers, at the time of submission. This had no impact on the peer review process and the final decision.

Publisher's note

Supplementary material

The Supplementary Material for this article can be found online at: https://www.frontiersin.org/articles/10.3389/fnano.2024.1483917/full#supplementary-material

References

Allen, N. S., Mahdjoub, N., Vishnyakov, V., Kelly, P. J., and Kriek, R. J. (2018). The effect of crystalline phase (anatase, brookite and rutile) and size on the photocatalytic activity of calcined polymorphic titanium dioxide (TiO2). *Polym. Degrad. Stab.* 150, 31–36. doi:10.1016/J.POLYMDEGRADSTAB.2018.02.008

Anpo, M., Shima, T., Kodama, S., and Kubokawa, Y. (1987). Photocatalytic hydrogenation of propyne with water on small-particle titania: size quantization effects and reaction intermediates. *J. Phys. Chem.* 91, 4305–4310. doi:10.1021/j100300a021

Appadurai, T., Subramaniyam, C. M., Kuppusamy, R., Karazhanov, S., and Subramanian, B. (2019). Electrochemical performance of nitrogen-doped TiO2 nanotubes as electrode material for supercapacitor and Li-ion battery. *Molecules* 24, 2952. doi:10.3390/molecules24162952

Asencios, Y. J. O., Lourenço, V. S., and Carvalho, W. A. (2022). Removal of phenol in seawater by heterogeneous photocatalysis using activated carbon materials modified with TiO2. *Catal. Today* 388–389, 247–258. doi:10.1016/J.CATTOD.2020.06.064

Asiltürk, M., and Şener, Ş. (2012). TiO2-activated carbon photocatalysts: preparation, characterization and photocatalytic activities. *Chem. Eng. J.* 180, 354–363. doi:10.1016/j.cej.2011.11.045

Ayala, J., Ramirez, D., Fletes, E., Morales, H., Parsons, J. G., and Alcoutlabi, M. (2021). Centrifugal spinning and characterization of CO3O4 coated carbon fibers. *Nano-Structures and Nano-Objects* 28, 100790. doi:10.1016/J.NANOSO.2021.100790

Bhatia, D., Sharma, N. R., Singh, J., and Kanwar, R. S. (2017). Biological methods for textile dye removal from wastewater: a review. *Crit. Rev. Environ. Sci. Technol.* 47, 1836–1876. doi:10.1080/10643389.2017.1393263

Binaeian, E., Seghatoleslami, N., Chaichi, M. J., and Tayebi, H. allah (2016). Preparation of titanium dioxide nanoparticles supported on hexagonal mesoporous silicate (HMS) modified by oak gall tannin and its photocatalytic performance in degradation of azo dye. *Adv. Powder Technol.* 27, 1047–1055. doi:10.1016/J.APT.2016.03.012

Cai, J., Hu, S., Xiang, J., Zhang, H., and Men, D. (2020). The effect of graphitized carbon on the adsorption and photocatalytic degradation of methylene blue over TiO2/C composites. *RSC Adv.* 10, 40830–40842. doi:10.1039/D0RA01105C

Cao, L., Zhou, X., Li, Z., Su, K., and Cheng, B. (2019). Nitrogen and fluorine hybridization state tuning in hierarchical honeycomb-like carbon nanofibers for optimized electrocatalytic ORR in alkaline and acidic electrolytes. *J. Power Sources* 413, 376–383. doi:10.1016/J.JPOWSOUR.2018.12.076

Chandra, M., Bhunia, K., and Pradhan, D. (2018). Controlled synthesis of CuS/TiO2 heterostructured nanocomposites for enhanced photocatalytic hydrogen generation through water splitting. *Inorg. Chem.* 57, 4524–4533. doi:10.1021/acs.inorgchem.8b00283

Chennam, P. K., Kachlík, M., Říhová, M., Čičmancová, V., Maca, K., and Macak, J. M. (2024). Synthesis of centrifugally spun polyacrylonitrile-carbon fibers. *J. Mater. Res. Technol.* 28, 2199–2205. doi:10.1016/J.JMRT.2023.12.146

Cui, G., Wang, W., Ma, M., Zhang, M., Xia, X., Han, F., et al. (2013). Rational design of carbon and TiO2 assembly materials: covered or strewn, which is better for photocatalysis? *Chem. Commun.* 49, 6415–6417. doi:10.1039/C3CC42500B

Davisdóttir, S., Shabadi, R., Galca, A. C., Andersen, I. H., Dirscherl, K., and Ambat, R. (2014). Investigation of DC magnetron-sputtered TiO2 coatings: effect of coating thickness, structure, and morphology on photocatalytic activity. *Appl. Surf. Sci.* 313, 677–686. doi:10.1016/J.APSUSC.2014.06.047

Djellabi, R., Ghorab, M. F., and Sehili, T. (2017). Simultaneous removal of methylene blue and hexavalent chromium from water using TiO2/Fe (III)/H2O2/sunlight. *CLEAN–Soil, Air, Water* 45, 1500379. doi:10.1002/clen.201500379

Dulmaa, A., Cougnon, F. G., Dedoncker, R., and Depla, D. (2021). On the grain size-thickness correlation for thin films. *Acta Mater* 212, 116896. doi:10.1016/J.ACTAMAT.2021.116896

El-Sayed, B. A., Mohamed, W. A. A., Galal, H. R., Abd El-Bary, H. M., and Ahmed, M. A. M. (2019). Photocatalytic study of some synthesized MWCNTs/TiO2 nanocomposites used in the treatment of industrial hazard materials. *Egypt. J. Petroleum* 28, 247–252. doi:10.1016/J.EJPE.2019.05.002

Farouk, H. U., Raman, A. A. A., and Daud, W. M. A. W. (2016). TiO2 catalyst deactivation in textile wastewater treatment: current challenges and future advances. *J. Industrial Eng. Chem.* 33, 11–21. doi:10.1016/J.JIEC.2015.10.022

Fujishima, A., Zhang, X., and Tryk, D. A. (2008). TiO2 photocatalysis and related surface phenomena. *Surf. Sci. Rep.* 63, 515–582. doi:10.1016/J.SURFREP.2008.10.001

Gaya, U. I., and Abdullah, A. H. (2008). Heterogeneous photocatalytic degradation of organic contaminants over titanium dioxide: a review of fundamentals, progress and problems. *J. Photochem. Photobiol. C Photochem. Rev.* 9, 1–12. doi:10.1016/J.JPHOTOCHEMREV.2007.12.003

Ghemid, M., Gueddaoui, H., Hemissi, M., Khelladi, M. R., and Bourzami, R. (2021). Thickness effect on structural, optoelectronic properties and photocatalytic activity of low-cost spin-coated In2O3 films. *Chem. Phys. Lett.* 784, 139089. doi:10.1016/j.cplett.2021.139089

Henderson, M. A. (2011). A surface science perspective on TiO2 photocatalysis. *Surf. Sci. Rep.* 66, 185–297. doi:10.1016/J.SURFREP.2011.01.001

Hir, Z. A. M., Moradihamedani, P., Abdullah, A. H., and Mohamed, M. A. (2017). Immobilization of TiO2 into polyethersulfone matrix as hybrid film photocatalyst for effective degradation of methyl orange dye. *Mater Sci. Semicond. Process* 57, 157–165. doi:10.1016/J.MSSP.2016.10.009

Hiremath, N., and Bhat, G. (2015). Melt blown polymeric nanofibers for medical applications-an overview. *Nanosci. Technol.* 2, 1–9. doi:10.15226/2374-8141/2/1/00125

Hitam, C. N. C., and Jalil, A. A. (2020). A review on exploration of Fe2O3 photocatalyst towards degradation of dyes and organic contaminants. *J. Environ. Manage* 258, 110050. doi:10.1016/J.JENVMAN.2019.110050

Hromádko, L., Koudelková, E., Bulánek, R., and Macak, J. M. (2017). SiO2 fibers by centrifugal spinning with excellent textural properties and water adsorption performance. *ACS Omega* 2, 5052–5059. doi:10.1021/acsomega.7b00770

Hromádko, L., Motola, M., Čičmancová, V., Bulánek, R., and Macak, J. M. (2021). Facile synthesis of WO3 fibers via centrifugal spinning as an efficient UV- and VIS-light-driven photocatalyst. *Ceram. Int.* 47, 35361–35365. doi:10.1016/J.CERAMINT.2021.09.079

Huang, Z. M., Zhang, Y. Z., Kotaki, M., and Ramakrishna, S. (2003). A review on polymer nanofibers by electrospinning and their applications in nanocomposites. *Compos Sci. Technol.* 63, 2223–2253. doi:10.1016/S0266-3538(03)00178-7

Ikegame, M., Tajima, K., and Aida, T. (2003). Template synthesis of polypyrrole nanofibers insulated within one-dimensional silicate channels: hexagonal versus lamellar for recombination of polarons into bipolarons. *Angew. Chem. Int. Ed.* 42, 2154–2157. doi:10.1002/anie.200250800

Keller, N., Rebmann, G., Barraud, E., Zahraa, O., and Keller, V. (2005). Macroscopic carbon nanofibers for use as photocatalyst support. *Catal. Today* 101, 323–329. doi:10.1016/J.CATTOD.2005.03.021

Kenanakis, G., Vernardou, D., Dalamagkas, A., and Katsarakis, N. (2015). Photocatalytic and electrooxidation properties of TiO2 thin films deposited by sol–gel. *Catal. Today* 240, 146–152. doi:10.1016/J.CATTOD.2014.05.007

Kievsky, Y., and Sokolov, I. (2005). Self-assembly of uniform nanoporous silica fibers. *IEEE Trans. Nanotechnol.* 4, 490–494. doi:10.1109/tnano.2005.851425

Kiran, V., and Sampath, S. (2012). Enhanced Raman spectroscopy of molecules adsorbed on carbon-doped TiO2 obtained from titanium carbide: a visible-light-assisted renewable substrate. *ACS Appl. Mater Interfaces* 4, 3818–3828. doi:10.1021/am300349k

Kumar, K. J., Raju, N. R. C., and Subrahmanyam, A. (2011). Thickness dependent physical and photocatalytic properties of ITO thin films prepared by reactive DC magnetron sputtering. *Appl. Surf. Sci.* 257, 3075–3080. doi:10.1016/J.APSUSC.2010.10.119

Lakshmipathi Naik, G. D., Kottam, N., and Shivashankar, G. K. (2010). Photo catalytic degradation of azo dyes over Mn2+ doped TiO2 catalyst under UV/solar light: an insight to the route of electron transfer in the mixed phase of anatase and rutile. *Chin. J. Chem.* 28, 2151–2161. doi:10.1002/cjoc.201090356

Langford, J.Il, and Wilson, A. J. C. (1978). Scherrer after sixty years: a survey and some new results in the determination of crystallite size. *J. Appl. Crystallogr.* 11, 102–113. doi:10.1107/s0021889878012844

Lee, K.-C., and Choo, K.-H. (2014). Optimization of flocculation conditions for the separation of TiO2 particles in coagulation-photocatalysis hybrid water treatment. *Chem. Eng. Process. Process Intensif.* 78, 11–16. doi:10.1016/j.cep.2014.01.010

Lee, S. S., Bai, H., Liu, Z., and Sun, D. D. (2015). Green approach for photocatalytic Cu(II)-EDTA degradation over TiO2: toward environmental sustainability. *Environ. Sci. Technol.* 49, 2541–2548. doi:10.1021/es504711e

Lin, L., Wang, H., Luo, H., and Xu, P. (2015). Enhanced photocatalysis using side-glowing optical fibers coated with Fe-doped TiO2 nanocomposite thin films. *J. Photochem Photobiol. A Chem.* 307–308, 88–98. doi:10.1016/J.JPHOTOCHEM.2015.04.010

Liu, H., Li, W., Shen, D., Zhao, D., and Wang, G. (2015). Graphitic carbon conformal coating of mesoporous TiO2 hollow spheres for high-performance lithium ion battery anodes. *J. Am. Chem. Soc.* 137, 13161–13166. doi:10.1021/jacs.5b08743

Lu, Y., Li, Y., Zhang, S., Xu, G., Fu, K., Lee, H., et al. (2013). Parameter study and characterization for polyacrylonitrile nanofibers fabricated via centrifugal spinning process. *Eur. Polym. J.* 49, 3834–3845. doi:10.1016/J.EURPOLYMJ.2013.09.017

Malaeb, L., and Ayoub, G. M. (2011). Reverse osmosis technology for water treatment: state of the art review. *Desalination* 267, 1–8. doi:10.1016/J.DESAL.2010.09.001

Malagutti, A. R., Mourão, H. A. J. L., Garbin, J. R., and Ribeiro, C. (2009). Deposition of TiO2 and Ag:TiO2 thin films by the polymeric precursor method and their application in the photodegradation of textile dyes. *Appl. Catal. B* 90, 205–212. doi:10.1016/J.APCATB.2009.03.014

Malik, P. K. (2004). Dye removal from wastewater using activated carbon developed from sawdust: adsorption equilibrium and kinetics. *J. Hazard Mater* 113, 81–88. doi:10.1016/J.JHAZMAT.2004.05.022

Marcano, D. C., Kosynkin, D. V., Berlin, J. M., Sinitskii, A., Sun, Z., Slesarev, A., et al. (2010). Improved synthesis of graphene oxide. *ACS Nano* 4, 4806–4814. doi:10.1021/nn1006368

McEachin, Z., and Lozano, K. (2012). Production and characterization of polycaprolactone nanofibers via forcespinning™ technology. *J. Appl. Polym. Sci.* 126, 473–479. doi:10.1002/app.36843

Mclaren, A., Valdes-Solis, T., Li, G., and Tsang, S. C. (2009). Shape and size effects of ZnO nanocrystals on photocatalytic activity. *J. Am. Chem. Soc.* 131, 12540–12541. doi:10.1021/ja9052703

Mihut, D. M., Lozano, K., and Foltz, H. (2014). Fabrication and characterization of silver- and copper-coated Nylon 6 forcespun nanofibers by thermal evaporation. *J. Vac. Sci. and Technol. A Vac. Surfaces, Films* 32, 61401. doi:10.1116/1.4896752

Mortazavi-Derazkola, S., Zinatloo-Ajabshir, S., and Salavati-Niasari, M. (2017). Facile hydrothermal and novel preparation of nanostructured Ho2O3 for photodegradation of eriochrome black T dye as water pollutant. *Adv. Powder Technol.* 28, 747–754. doi:10.1016/J.APT.2016.11.022

Muñoz-Fernandez, L., Sierra-Fernandez, A., Milošević, O., and Rabanal, M. E. (2016). Solvothermal synthesis of Ag/ZnO and Pt/ZnO nanocomposites and comparison of their photocatalytic behaviors on dyes degradation. *Adv. Powder Technol.* 27, 983–993. doi:10.1016/J.APT.2016.03.021

Naeimirad, M., Zadhoush, A., Kotek, R., Esmaeely Neisiany, R., Nouri Khorasani, S., and Ramakrishna, S. (2018). Recent advances in core/shell bicomponent fibers and nanofibers: a review. *J. Appl. Polym. Sci.* 135, 46265. doi:10.1002/app.46265

Naidi, S. N., Harunsani, M. H., Tan, A. L., and Khan, M. M. (2021). Green-synthesized CeO2 nanoparticles for photocatalytic, antimicrobial, antioxidant and cytotoxicity activities. *J. Mater Chem. B* 9, 5599–5620. doi:10.1039/D1TB00248A

Natarajan, T. S., and Bhargava, P. (2018). Influence of spinning parameters on synthesis of alumina fibres by centrifugal spinning. *Ceram. Int.* 44, 11644–11649. doi:10.1016/J.CERAMINT.2018.03.239

Ong, C. B., Ng, L. Y., and Mohammad, A. W. (2018). A review of ZnO nanoparticles as solar photocatalysts: synthesis, mechanisms and applications. *Renew. Sustain. Energy Rev.* 81, 536–551. doi:10.1016/J.RSER.2017.08.020

Pala, A., and Tokat, E. (2002). Color removal from cotton textile industry wastewater in an activated sludge system with various additives. *Water Res.* 36, 2920–2925. doi:10.1016/S0043-1354(01)00529-2

Pandimurugan, R., and Thambidurai, S. (2016). Novel seaweed capped ZnO nanoparticles for effective dye photodegradation and antibacterial activity. *Adv. Powder Technol.* 27, 1062–1072. doi:10.1016/J.APT.2016.03.014

Parrott, J. L., Bartlett, A. J., and Balakrishnan, V. K. (2016). Chronic toxicity of azo and anthracenedione dyes to embryo-larval fathead minnow. *Environ. Pollut.* 210, 40–47. doi:10.1016/J.ENVPOL.2015.11.037

Parvizi, E., Tayebee, R., Koushki, E., Abdizadeh, M. F., Maleki, B., Audebert, P., et al. (2019). Photocatalytic efficacy of supported tetrazine on MgZnO nanoparticles for the heterogeneous photodegradation of methylene blue and ciprofloxacin. *RSC Adv.* 9, 23818–23831. doi:10.1039/c9ra04702f

Prakash, K., Senthil Kumar, P., Pandiaraj, S., Saravanakumar, K., and Karuthapandian, S. (2016). Controllable synthesis of SnO2 photocatalyst with superior photocatalytic activity for the degradation of methylene blue dye solution. *J. Exp. Nanosci.* 11, 1138–1155. doi:10.1080/17458080.2016.1188222

Quici, N., Vera, M. L., Choi, H., Puma, G. L., Dionysiou, D. D., Litter, M. I., et al. (2010). Effect of key parameters on the photocatalytic oxidation of toluene at low concentrations in air under 254 + 185 nm UV irradiation. *Appl. Catal. B* 95, 312–319. doi:10.1016/J.APCATB.2010.01.009

Rajeshwar, K., Osugi, M. E., Chanmanee, W., Chenthamarakshan, C. R., Zanoni, M. V. B., Kajitvichyanukul, P., et al. (2008). Heterogeneous photocatalytic treatment of organic dyes in air and aqueous media. *J. Photochem. Photobiol. C Photochem. Rev.* 9, 171–192. doi:10.1016/J.JPHOTOCHEMREV.2008.09.001

Rihova, M., Ince, A. E., Cicmancova, V., Hromadko, L., Castkova, K., Pavlinak, D., et al. (2021). Water-born 3D nanofiber mats using cost-effective centrifugal spinning: comparison with electrospinning process: a complex study. *J. Appl. Polym. Sci.* 138. doi:10.1002/app.49975

Rihova, M., Lepcio, P., Cicmancova, V., Frumarova, B., Hromadko, L., Bureš, F., et al. (2022). The centrifugal spinning of vitamin doped natural gum fibers for skin regeneration. *Carbohydr. Polym.* 294, 119792. doi:10.1016/J.CARBPOL.2022.119792

Samai, B., and Bhattacharya, S. C. (2018). Conducting polymer supported cerium oxide nanoparticle: enhanced photocatalytic activity for waste water treatment. *Mater Chem. Phys.* 220, 171–181. doi:10.1016/j.matchemphys.2018.08.050

Sarkar, K., Gomez, C., Zambrano, S., Ramirez, M., De Hoyos, E., Vasquez, H., et al. (2010). Electrospinning to Forcespinning™. *Mater. Today* 13, 12–14. doi:10.1016/S1369-7021(10)70199-1

Schneider, J., Matsuoka, M., Takeuchi, M., Zhang, J., Horiuchi, Y., Anpo, M., et al. (2014). Understanding TiO2 photocatalysis: mechanisms and materials. *Chem. Rev.* 114, 9919–9986. doi:10.1021/cr5001892

Shakouri, A., Heris, S. Z., Etemad, S. G., and Mousavi, S. M. (2016). Photocatalytic activity performance of novel cross-linked PEBAX copolymer nanocomposite on azo dye degradation. *J. Mol. Liq.* 216, 275–283. doi:10.1016/J.MOLLIQ.2016.01.008

Shan, A. Y., Ghazi, T. I. M., and Rashid, S. A. (2010). Immobilisation of titanium dioxide onto supporting materials in heterogeneous photocatalysis: a review. *Appl. Catal. A Gen.* 389, 1–8. doi:10.1016/J.APCATA.2010.08.053

Smirnov, M., Baban, C., and Rusu, G. I. (2010). Structural and optical characteristics of spin-coated ZnO thin films. *Appl. Surf. Sci.* 256, 2405–2408. doi:10.1016/J.APSUSC.2009.10.075

Sobana, N., Thirumalai, K., and Swaminathan, M. (2016). Kinetics of solar light assisted degradation of direct red 23 on activated carbon-loaded zinc oxide and influence of operational parameters. *Trans* 4, 77–89.

Sopha, H., Krbal, M., Ng, S., Prikryl, J., Zazpe, R., Yam, F. K., et al. (2017). Highly efficient photoelectrochemical and photocatalytic anodic TiO2 nanotube layers with additional TiO2 coating. *Appl. Mater Today* 9, 104–110. doi:10.1016/J.APMT.2017.06.002

Sopha, H., Mirza, I., Turčičova, H., Pavlinak, D., Michalicka, J., Krbal, M., et al. (2020). Laser-induced crystallization of anodic TiO2 nanotube layers. *RSC Adv.* 10, 22137–22145. doi:10.1039/D0RA02929G

Subramanian, V., Kamat, P. V., and Wolf, E. E. (2003). Mass-transfer and kinetic studies during the photocatalytic degradation of an azo dye on optically transparent electrode thin film. *Ind. Eng. Chem. Res.* 42, 2131–2138. doi:10.1021/ie020636u

Swamy, V., Menzies, D., Muddle, B. C., Kuznetsov, A., Dubrovinsky, L. S., Dai, Q., et al. (2006). Nonlinear size dependence of anatase TiO2 lattice parameters. *Appl. Phys. Lett.* 88, 243103. doi:10.1063/1.2213956

Tahir, M., Alesayi, M. T. H., and Alshehhi, S. M. S. (2023). Recycling carbon fiber-reinforced polymers (CFRPs) to construct CFs/TiO2 nanotexture with efficient interface charge transfer for stimulating photocatalytic hydrogen production. *Energy and Fuels* 37, 12319–12334. doi:10.1021/acs.energyfuels.3c01333

Takeda, N., Iwata, N., Torimoto, T., and Yoneyama, H. (1998). Influence of carbon black as an adsorbent used in TiO2 photocatalyst films on photodegradation behaviors of propyzamide. *J. Catal.* 177, 240–246. doi:10.1006/JCAT.1998.2117

Teng, F., Zhang, G., Wang, Y., Gao, C., Chen, L., Zhang, P., et al. (2014). The role of carbon in the photocatalytic reaction of carbon/TiO2 photocatalysts. *Appl. Surf. Sci.* 320, 703–709. doi:10.1016/J.APSUSC.2014.09.153

Thalluri, S. M., Rodriguez-Pereira, J., Zazpe, R., Bawab, B., Kolíbalová, E., Jelinek, L., et al. (2023). Enhanced CO functionality on carbon papers ensures lowering nucleation delay of ALD for Ru towards unprecedented alkaline HER activity. *Small* 19, 2300974. doi:10.1002/smll.202300974

Tsai, S. J., and Cheng, S. (1997). Effect of TiO2 crystalline structure in photocatalytic degradation of phenolic contaminants. *Catal. Today* 33, 227–237. doi:10.1016/S0920-5861(96)00152-6

Vazquez, B., Vasquez, H., and Lozano, K. (2012). Preparation and characterization of polyvinylidene fluoride nanofibrous membranes by forcespinning™. *Polym. Eng. Sci.* 52, 2260–2265. doi:10.1002/pen.23169

Wang, X., Sø, L., Su, R., Wendt, S., Hald, P., Mamakhel, A., et al. (2014). The influence of crystallite size and crystallinity of anatase nanoparticles on the photo-degradation of phenol. *J. Catal.* 310, 100–108. doi:10.1016/J.JCAT.2013.04.022

Wu, C. Y., Lee, Y. L., Lo, Y. S., Lin, C. J., and Wu, C. H. (2013). Thickness-dependent photocatalytic performance of nanocrystalline TiO2 thin films prepared by sol–gel spin coating. *Appl. Surf. Sci.* 280, 737–744. doi:10.1016/J.APSUSC.2013.05.053

Xie, M., Jing, L., Zhou, J., Lin, J., and Fu, H. (2010). Synthesis of nanocrystalline anatase TiO2 by one-pot two-phase separated hydrolysis-solvothermal processes and its high activity for photocatalytic degradation of rhodamine B. *J. Hazard Mater* 176, 139–145. doi:10.1016/J.JHAZMAT.2009.11.008

Xu, N., Shi, Z., Fan, Y., Dong, J., Shi, J., and Hu, M. Z.-C. (1999). Effects of particle size of TiO2 on photocatalytic degradation of methylene blue in aqueous suspensions. *Ind. Eng. Chem. Res.* 38, 373–379. doi:10.1021/ie980378u

Yanagisawa, K., and Ovenstone, J. (1999). Crystallization of anatase from amorphous titania using the hydrothermal technique: effects of starting material and temperature. *J. Phys. Chem. B* 103, 7781–7787. doi:10.1021/jp990521c

Ye, X., Li, Z., Sun, H., Wu, M., An, Z., Pang, Y., et al. (2022). Incorporating TiO2 nanoparticles into the multichannels of electrospun carbon fibers to increase the adsorption of polysulfides in room temperature sodium-sulfur batteries. *New Carbon Mater.* 37, 1116–1122. doi:10.1016/S1872-5805(22)60607-3

Yeung, K. L., Maira, A. J., Stolz, J., Hung, E., Ka-Chun Ho, N., Wei, A. C., et al. (2002). Ensemble effects in nanostructured TiO2 used in the gas-phase photooxidation of trichloroethylene. *J. Phys. Chem. B* 106, 4608–4616. doi:10.1021/jp0131121

Yu, J., Wang, G., Cheng, B., and Zhou, M. (2007). Effects of hydrothermal temperature and time on the photocatalytic activity and microstructures of bimodal mesoporous TiO2 powders. *Appl. Catal. B* 69, 171–180. doi:10.1016/J.APCATB.2006.06.022

Zhao, J., Han, W., Chen, H., Tu, M., Zeng, R., Shi, Y., et al. (2011). Preparation, structure and crystallinity of chitosan nano-fibers by a solid–liquid phase separation technique. *Carbohydr. Polym.* 83, 1541–1546. doi:10.1016/J.CARBPOL.2010.10.009